International Journal of Mass Spectrometry 275 (2008) 11–20

Contents lists available at ScienceDirect

International Journal of Mass Spectrometry

journal homepage: www.elsevier.com/locate/ijms

Numerical observation of preferred directionality in ion ejection from stretched rectilinear ion traps

A. Krishnaveni [a], Neeraj Kumar Verma [b], A.G. Menon [a], Atanu K. Mohanty [a,b,*]

[a] Department of Instrumentation, Indian Institute of Science, Bangalore 560012, India
[b] Supercomputer Education and Research Centre, Indian Institute of Science, Bangalore 560012, India

ARTICLE INFO

Article history:
Received 7 February 2008
Received in revised form 3 May 2008
Accepted 3 May 2008
Available online 16 May 2008

Keywords:
Rectilinear ion trap
Nonlinear ion trap
Stretched geometry
Directionality of ion ejection
Boundary element method (BEM)

ABSTRACT

We report on numerical investigations of directionality of ion ejection in stretched rectilinear ion traps (RIT). Three 4-electrode trap geometries have been investigated. In all cases, one pair of electrodes has slits at their center and the other pair has no slits. The studied traps include the RIT-S, in which the mass analyzer electrodes are symmetrically positioned around the central axis; the RIT-X, in which the mass analyzer has a stretch in the direction of the electrodes which have slits (labeled as *x*-direction); and the RIT-Y, in which the mass analyzer has a stretch in the direction of the electrodes which have no slits (labeled as *y*-direction).

Our analysis has been carried out on two-dimensional (2D) fields at the centre of an infinitely long mass analyzer. The boundary element method (BEM) has been used for field computations. The trajectory of ion motion has been generated using Runge Kutta fourth order integration.

Three sets of simulations have been carried out on each of the RIT-S, the RIT-X and the RIT-Y to check for directionality of ion ejection. In the first, we numerically obtain the stability region on the potential (U_{dc}– V_{rf}) axes. In the second we generate an escape velocity plot with $U_{dc} = 0$ for different values of V_{rf}. In the third, we simulate the mass selective boundary ejection experiment on a single ion.

In the symmetric RIT-S, as expected, all three simulations show that there is an equal probability of ion reaching the trap boundary in either of the *x*- or *y*-directions. For the stretched traps, however, the results are dramatically different. For the RIT-X, all three simulations suggest that ion destabilization at the stability boundary occurs in the *x*-direction. Similarly, for the RIT-Y, ions preferentially get destabilized in the *y*-direction. That is, ions reaching the trap boundary overwhelmingly prefer the stretch direction.

1. Introduction

The rectilinear ion trap (RIT) mass spectrometer, invented by Cooks and co-workers [19,32], has a 6-electrode mass analyzer with four planar rectangular electrodes (arranged symmetrically around the central axis) constituting the central section and two flat electrodes, facing the central section, forming the endcaps. The geometry of the RIT is a simplification of the geometry of the linear ion trap (LIT) [3], which has a four hyperbolic rod central section and two electrically isolated segments of the central section acting as the endcap electrodes. Both the LIT and the RIT are two-dimensional (2D) analogs of the well known three-dimensional (3D) Paul trap [20]. For the trap operation, the two opposite pairs of electrodes in the central section are each electrically shorted and trapping is effected by application of rf-only or rf/dc potential across the pairs. Trapping in the axial direction is achieved by application of a dc potential on the endcaps.

Two major advantages that the LIT has over its 3D counterpart are its greatly improved trapping efficiency [6,12,23] and its enhanced sensitivity [24,22]. It is to utilize these features in a miniaturizable structure that Ouyang et al. [19] conceived the RIT.

To improve the performance of the LIT and the RIT, researchers have modified the field within the trap. These modifications introduced a cubic (octopole) term in the field to overcome the deleterious effect of the square (hexapole) term in the field, a lesson learnt from the 3D Paul trap where "stretching" of the geometry from its ideal configuration improved machine performance [29]. To increase the fragmentation efficiency Collings [4] introduced extra electrodes in between the circular rods of the LIT and Michaud et al. [18] used two different rod diameters to study its effect on the trap performance. For the RIT, Ouyang et al. [19] and Zhang et al. [32] have stretched the central section in one direction to obtain

* Corresponding author at: Supercomputer Education and Research Centre, Indian Institute of Science, Bangalore 560012, India. Tel.: +91 80 2293 2979; fax: +91 80 2360 0135.
E-mail addresses: krishnasai@isu.iisc.ernet.in (A. Krishnaveni), neeraj@rishi.serc.iisc.ernet.in (N. Kumar Verma), agmenon@isu.iisc.ernet.in (A.G. Menon), amohanty@serc.iisc.ernet.in (A.K. Mohanty).

1387-3806/$ – see front matter © 2008 Elsevier B.V. All rights reserved.
doi:10.1016/j.ijms.2008.05.011

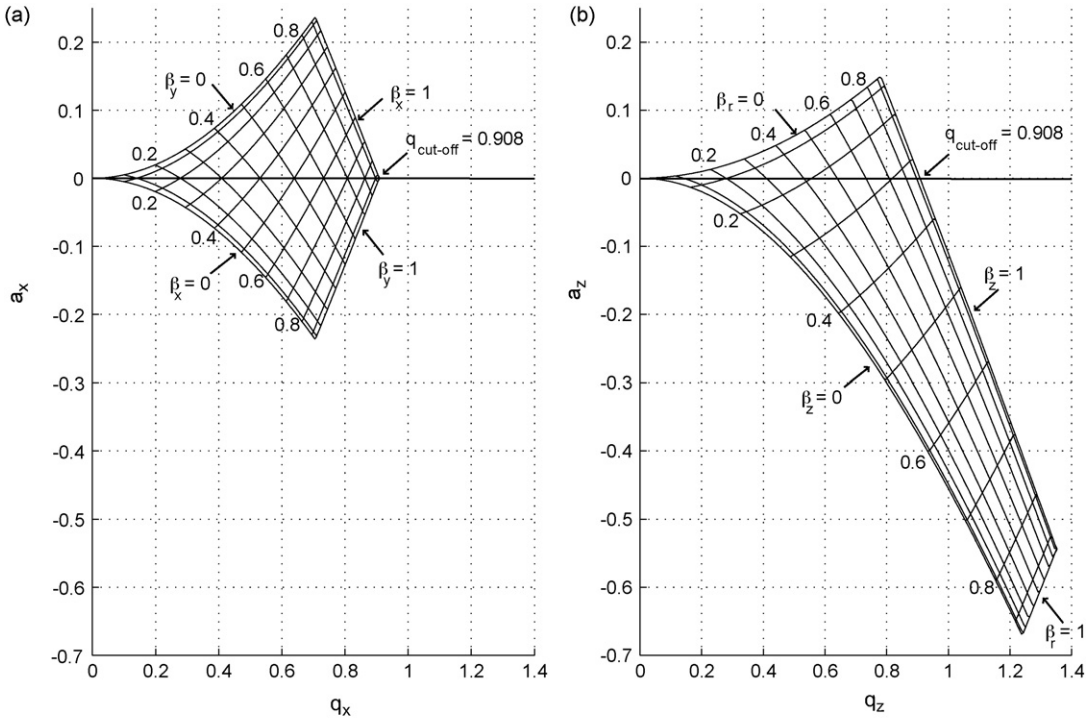

Fig. 1. Mathieu stability plots for (a) the LIT and (b) the 3D Paul trap.

improved resolution in mass spectra for resonance ejection experiments. Similar results were reported in a stretched RIT in resonance ejection experiments by [27] using their 4-electrode RIT [26].

For the ideal LIT, the equations of ion motion in the x- and y-directions (see Fig. 2 for the directions in the RIT) are two uncoupled linear Mathieu equations given by [5]

$$\frac{d^2u}{d\xi^2} + (a_u - 2q_u \cos 2\xi)u = 0 \quad (1)$$

where

$$a_x = -a_y = \frac{8eA_2U_{dc}}{mr_0^2\Omega^2} \quad \text{and} \quad q_x = -q_y = \frac{4eA_2V_{rf}}{mr_0^2\Omega^2} \quad (2)$$

In Eqs. (1) and (2) a_u and q_u are Mathieu parameters where u represents the x- or y-directions, Ω is the angular frequency of the rf drive, $\xi = \Omega t/2$ is dimensionless time, t is time, A_2 is the weight of the linear field, U_{dc} and V_{rf} are the dc and rf potentials applied across the two pairs of electrodes, respectively, e/m is the charge-to-mass ratio of the ion, and r_0 is a normalizing length.

The stability of ions in the LIT can be depicted on a Mathieu stability plot using parameters a_u and q_u (a_x– q_x for the 2D LIT and a_z– q_z for the 3D Paul trap). Fig. 1(a) delineates the region on the a_x– q_x plane where both x- and y-direction motions are stable for the LIT. Also shown for comparison, in Fig. 1(b), is the stable region for the 3D Paul trap (see March and Hughes [17] for definitions of a_z and q_z for the 3D trap). It can be seen in the figures that the stable region is bounded by values of β_u between 0 and 1 (β_u is a parameter related to Mathieu parameters a_u and q_u by a continued fraction relationship [17]).

In mass selective boundary ejection experiments [33], the trap is operated on the $a_u = 0$ line and ion destabilization occurs when its q_u value crosses the stability boundary at $q_{cut-off}$. In 3D Paul traps ion destabilization occurs at the $\beta_z = 1$ curve (Fig. 1(b)) resulting in ion ejection in the axial (z)-direction. In the ideal LIT, on the other hand, ions which are trapped along the z-axis are destabilized in the x–y plane when their q_x or q_y reaches $q_{cut-off}$ (Fig. 1(a)). Here, since both $\beta_x = 1$ and $\beta_y = 1$ intersect the $a_x = 0$ line simultaneously at $q_{cut-off}$, there is an equal probability for ion exit in the x- and y-directions.

When the fields within the trap are weakly nonlinear, as they are in practical traps, the Mathieu stability plot gets distorted and, for the 2D trap, this is likely to impact the direction in which ions get ejected. This is not so for the 3D trap. For the 3D trap, considerable research exists on understanding changes in the stability region due to space charge [9,5,11] as well as due to field inhomogeneities [2,13,25,28,21]. All these reports have discussed the distortions of the stability region which, in the mass selective boundary ejection experiments, would result in destabilization still occurring *near* the nominal $\beta_z = 1$curve. For the 3D Paul traps, since the nominal ejection point near the $\beta_z = 1$ curve is far from the $\beta_r = 1$ ejection curve, ejection continues to primarily occur in the z-direction (perhaps slightly earlier or later, an issue that has been dealt with in the references cited above). In contrast, for the LIT, small nonideal effects can call into play either of the $\beta_x = 1$ or $\beta_y = 1$ curves, showing that *directionality* of ejection is an important issue. We observe that adding a dc voltage to the rf excitation in Fig. 1(a) would in principle lead to preferential ejection in one direction, as also mentioned in passing by Lammert et al. [15]. However, in this study, we consider no dc and confine attention to operation along $U_{dc} = 0$ line (i.e., along the q_x axis).

The present study investigates the direction of ion ejection in the RIT. To do this we have taken up for investigation RITs of three different geometries. In these geometries, we have assumed that the flat planar electrodes are infinitely long. Further, we assume that one pair of electrodes has slits in them at the centre, and the other pair of electrode has no slits. Of the three RITs, one has a symmetric design similar to that reported by Ouyang et al. [19], and the other two have stretched geometries, one having a stretch in the direction of electrode which have slits and the other having a stretch in the direction of electrode which have no slits.

A study of the ion dynamics in these three geometries will help us identify the preferred direction of ion destabilization in these instruments.

Our analysis has been carried out on two-dimensional (2D) fields at the centre of an infinitely long mass analyzer. The boundary element method (BEM) has been used for field computations. The trajectory of ion motion has been generated using Runge Kutta fourth order integration.

Three numerical experiments have been carried out here for each of the three geometries. In the first, we generate the stability plot to delineate the ranges of the rf and dc potentials within which ion motion is stable. The second set of simulations generates escape velocity plots for different value of rf with $U_{dc} = 0$. This will be used to provide additional evidence in our study of directionality of ion ejection, in addition to indicating nonlinear resonances which could effectively be used in resonance ejection experiments. Finally, we simulate the mass selective boundary ejection experiment to generate statistics to check for the directionality of ion destabilization in the three RITs.

Note that the mass selective boundary ejection experiment, unlike the resonance ejection experiment in which the ions are naturally predisposed to distabilize in the direction of applied ac auxiliary excitation, provides a suitable simulation environment to study direction of distabilization of ions in the RITs. While the first two simulations present general characteristics of the trap, the third simulation addresses the behavior of ions in only mass selective boundary ejection experiments and not other modes of operation such as resonance ejection [23] or axial ejection experiments [16].

In the next section, we present the geometries we have investigated. Following this, in Section 3, the computational methods used will be discussed. These will include charge and potential calculations and methods for generating stability plot and escape velocity curves. Section 4 presents the results of our computations. Concluding remarks are given in Section 5. Also provided in the appendix are the verification of the different numerical techniques adopted in the study.

2. Geometries considered

The cross-sectional view of the RITs taken up for numerical investigations is presented in Fig. 2. In the figure, w is the half-distance between the electrode in the x-direction, h is the half-distance between the electrode in the y-direction, x_s and y_s are the gaps between the electrodes in the x- and y-directions, respectively, h_s is the width of the slit in the electrodes and p is the width of the electrode.

By varying w and h we obtained the three RIT geometries which have been investigated in the present study. In the first, when $w = h$, we get a symmetric RIT and in this paper we have referred to it as RIT-S. The second geometry we have investigated is where $w > h$, and since this has a stretch in the x-direction, it is labeled as RIT-X. In the third geometry, where $w < h$, there is a stretch in the y-direction and we have labeled it as RIT-Y.

The parameters which are common to all geometries are h_s, and p and these dimensions are fixed as 1 and 7 mm, respectively. Since w and h vary in these three geometries, the parameters x_s and y_s also vary. The geometry parameters used for the three traps investigated are given in Table 1.

3. Computational methods

In this section we present salient features of the computational methods used by us. We first introduce the methods for computing the field and the multipole coefficients. Next, we present the method used for the determination of ion trajectories. Finally, we describe the method for numerically determining the stability region and the escape velocity diagram of the trap.

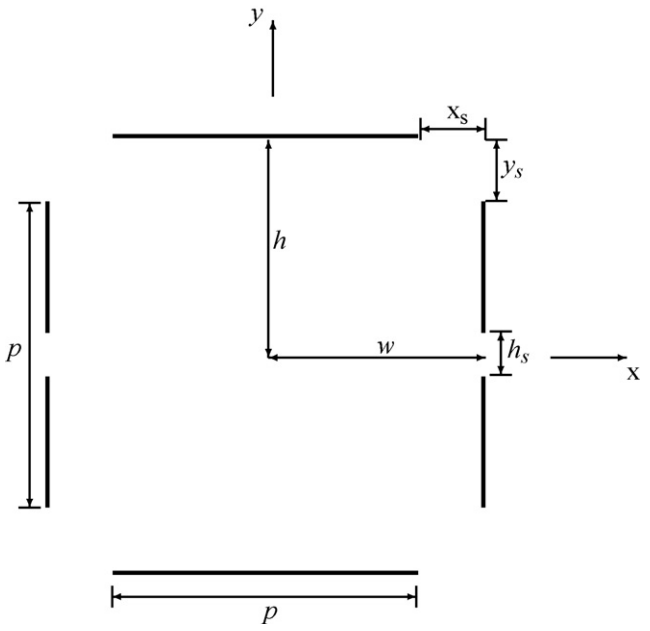

Fig. 2. Geometry parameters of the RIT.

In this study we have assumed that the electrodes of the mass analyzer are infinitely long. This enables us to carry out a 2D analysis of the trap for ion motion close to the centre of the trap. For the problem at hand the 2D analysis is considerably faster than a full 3D analysis.

3.1. Field computation using the BEM

In the present problem, the potentials on a number of conducting electrodes are specified. The field and potential at any given point in space needs to be computed. In the BEM this is achieved by first determining the unknown charge distribution on the electrodes. Once the charge distribution is known, the field and the potential anywhere in space are computed by superposition. In this study the cross-sections of the electrodes remain invariant in one direction with translation in the axial direction. So a two-dimensional formulation which requires less computation than a full three-dimensional formulation is used.

The electrodes are divided into a number of narrow strip elements for the BEM solution. Let the total number of elements be N. For the i-th element let $\mathbf{r}_i$ be the location, V_i be the applied potential, and q_i be the unknown charge belonging to the element. Let $G_{ij} \equiv G_{ij}(\mathbf{r}_i, \mathbf{r}_j)$ be the potential at element i due to unit charge at element j. The G_{ij} are known as the charge to potential Green's functions. Then the potential at element i due to all the N element charges is $\sum_{j=1}^{N} G_{ij} q_j$. Since the applied potential at element i is V_i.

Table 1
Geometry parameters of the RIT studied

	w	h	x_s	y_s	h_s	p
RIT-S	5.0	5.0	1.5	1.5	1.0	7.0
RIT-X	5.0	3.5	1.5	0.0	1.0	7.0
RIT-Y	3.5	5.0	0.0	1.5	1.0	7.0

All dimensions are in mm.

We have

$$\sum_{j=1}^{N} G_{ij} q_j = V_i, \quad i = 1, \ldots, N \tag{3}$$

The above system of N equations can be solved to determine the N unknown element charges $q_j, j = 1, \ldots, N$. For the computation of G_{ij} for $i \neq j$ the charge at element j can be regarded as a point charge. But for the computation of G_{ii} it is necessary to consider the charge on the element to be distributed over the entire width in order to avoid a singularity in the integral. The expression for computing G_{ij} will be discussed next.

3.1.1. Two-dimensional Green's functions

The computation of two-dimensional Green's function requires the computation of potentials due to line charges. The field at point (x, y) due to a line charge at (x_i, y_i) is given by [31]

$$\mathbf{E} = \frac{q_l}{2\pi\epsilon_o} \frac{\hat{x}(x - x_i) + \hat{y}(y - y_i)}{(x - x_i)^2 + (y - y_i)^2} \tag{4}$$

where q_l is the charge per unit length of the line charge. A suitable potential function satisfying $\mathbf{E} = -\nabla V$ is

$$V(x, y) = \frac{q_l}{2\pi\epsilon_o} \ln \frac{\rho_0}{\rho} \tag{5}$$

where $\rho = \sqrt{(x - x_i)^2 + (y - y_i)^2}$ is the distance from the line charge and the distance ρ_0 is an arbitrary constant.

The potential at distance ρ from a line charge q is proportional to $q \ln(\rho_0/\rho)$ which is unbounded as ρ tends to infinity. Therefore, the reference point for zero potential cannot be taken at infinity as in 3D problems. Consequently, a cylinder with a sufficiently large radius (large enough, say, to contain all the electrode including the vacuum chamber) is taken as the surface having zero potential. The Green's function for a line charge including the effect of the reference cylinder for $i \neq j$, is given by,

$$G_{ij} = \frac{1}{4\pi\epsilon_o} \ln \frac{(\rho_i \rho_j / R)^2 + R^2 - 2\rho_i \rho_j \cos(\phi_i - \phi_j)}{\rho_i^2 + \rho_j^2 - 2\rho_i \rho_j \cos(\phi_i - \phi_j)} \tag{6}$$

where (ρ_i, ϕ_i), (ρ_j, ϕ_j) are the polar coordinates of the centres of the i-th and the j-th elements, and R is the radius of the reference cylinder. Note that $G_{ij} = G_{ji}$. For $i = j$,

$$G_{ii} = \frac{1}{4\pi\epsilon_o} \left(2 + 2 \ln \frac{R - \rho_i^2/R}{w_i/2} \right) \tag{7}$$

where w_i is the width of element i.

3.2. Multipole coefficients

To calculate the weights of the multipole coefficients directly from the charge distribution, we first consider the general expression for a 2D potential in a polar coordinate system, which is given by,

$$\Phi(\rho, \phi) = \sum_{n=0}^{\infty} \rho^n (a_n \cos(n\phi) + b_n \sin(n\phi)) \tag{8}$$

$$\Phi(\rho, \phi) = \Phi_0 \sum_{n=0}^{\infty} \left(\frac{\rho}{r_0} \right)^n (A_n \cos(n\phi) + B_n \sin(n\phi)) \tag{9}$$

Here a_n, b_n correspond to the weights of the multipoles and are referred to as multipole coefficients; ρ, ϕ are the cylindrical polar coordinates, and Φ_0 is the applied potential difference across the pairs of trap electrodes. In the mass spectroscopy literature, however, the normalized coefficients A_n and B_n are frequently used (and referred to as multipole coefficient) because they are dimensionless and do not change when the size of a trap is scaled. The length scale r_0 used for normalization is a length indicating the size of the trap. In the classical LIT, r_0 is taken as the nearest distance from the centre of the trap to the electrodes, but in traps with nonhyperbolic electrodes the selection of r_0 is somewhat arbitrary. The normalized multipole coefficients are related to the unnormalized ones by

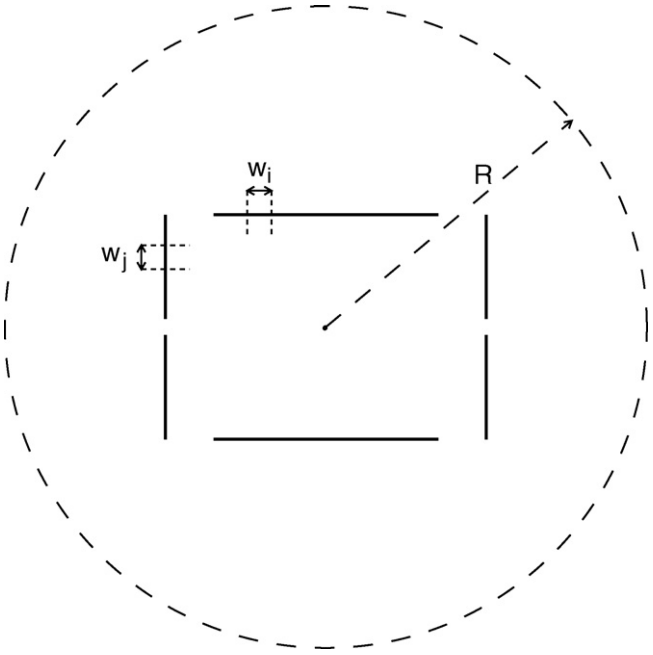

Fig. 3. Cross-sectional view of the RIT with the widths of the two segments indicated. Also shown in the diagram (as a dashed circle) is the imaginary cylindrical electrode positioned at radius R from the center of the trap.

$$A_n = \frac{a_n r_0^n}{\Phi_0} \tag{10}$$

$$B_n = \frac{b_n r_0^n}{\Phi_0} \tag{11}$$

Eq. (8) can be expanded as,

$$\Phi(\rho, \phi) = a_0 + \rho(a_1 \cos(\phi) + b_1 \sin(\phi)) + \rho^2(a_2 \cos(2\phi) + b_2 \sin(2\phi)) \ldots \tag{12}$$

Now, at a distance far away from the electrode, the strip w_i in Fig. 3 can be visualized as a straight wire. The electric potential, Φ at a point (ρ, ϕ) from such a straight wire, which has uniform line charge, q_i, and is located at (ρ_i, ϕ_i), is given as

$$\Phi = \frac{q_i}{4\pi\epsilon_o} \ln \frac{(\rho_i \rho / R)^2 + R^2 - 2\rho_i \rho \cos(\phi - \phi_i)}{\rho_i^2 + \rho^2 - 2\rho_i \rho \cos(\phi - \phi_i)} \tag{13}$$

Fig. 4 shows the location of the line charge (ρ_i, ϕ_i) on the electrode and an arbitrary point (ρ, ϕ) at which the potential is to be calculated.

By simplifying Eq. (13), we get

$$\Phi(\rho, \phi) = \frac{q_i}{4\pi\epsilon_o} \ln \frac{R^2}{\rho_i^2} \frac{1 + (\rho_i \rho / R^2)^2 - 2(\rho \rho_i / R^2) \cos(\phi - \phi_i)}{1 + (\rho/\rho_i)^2 - 2(\rho/\rho_i) \cos(\phi - \phi_i)} \tag{14}$$

We note that

$$\rho_{i'} = \frac{R^2}{\rho_i} \tag{15}$$

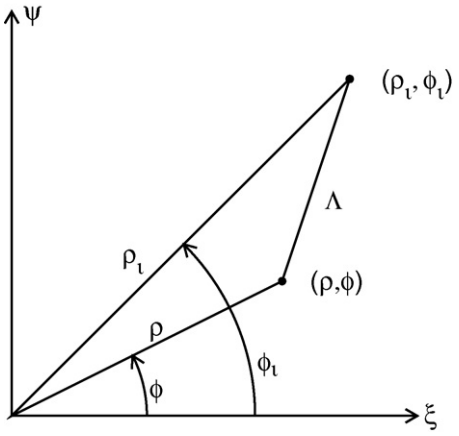

Fig. 4. Location of the strip at (ρ_i, ϕ_i) with respect to coordinates (ρ, ϕ) where the charge and the potential are to be computed.

is the distance of the image line charge from the origin. Then

$$\Phi = \frac{q_i}{4\pi\epsilon_o} \ln \frac{\rho_{i'}}{\rho_i} + \frac{q_i}{4\pi\epsilon_o} \ln \frac{1 + (\rho/\rho_{i'})^2 - 2(\rho/\rho_{i'})\cos(\phi - \phi_i)}{1 + (\rho/\rho_i)^2 - 2(\rho/\rho_i)\cos(\phi - \phi_i)} \tag{16}$$

By simplifying the logarithm in the second term of the Eq. (16) using

$$\ln(1 + t^2 - 2t\cos(\alpha)) = -2\sum_{n=1}^{\infty} \frac{t^n \cos(n\alpha)}{n} \tag{17}$$

we get

$$\Phi = \frac{q_i}{4\pi\epsilon_o} \left(\ln \frac{\rho_{i'}}{\rho_i} + \sum_{n=1}^{\infty} \frac{2\rho^n}{n} \left(\frac{1}{\rho_i^n} - \frac{1}{\rho_{i'}^n} \right) \times (\cos(n\phi_i)\cos(n\phi) + \sin(n\phi_i)\sin(n\phi)) \right) \tag{18}$$

Total potential at (ρ, ϕ) is found by accumulating the contribution due to all charge strips. The expression for total potential, due to N charge strips, is given by

$$\Phi = \sum_{i=1}^{N} \frac{q_i}{4\pi\epsilon_o} \left(\ln \frac{\rho_{i'}}{\rho_i} + \sum_{n=1}^{\infty} \frac{2\rho^n}{n} \left(\frac{1}{\rho_i^n} - \frac{1}{\rho_{i'}^n} \right) \times (\cos(n\phi_i)\cos(n\phi) + \sin(n\phi_i)\sin(n\phi)) \right) \tag{19}$$

In order to obtain the multipole weights from the charge, we compare Eq. (19) with Eq. (8). This yields

$$a_0 = \frac{1}{4\pi\epsilon_o} \sum_{i=1}^{N} q_i \ln \frac{\rho_{i'}}{\rho_i} \tag{20}$$

and,

$$a_n = \frac{1}{4\pi\epsilon_o} \sum_{i=1}^{N} \frac{2q_i \cos(n\phi_i)}{n} \left(\frac{1}{\rho_i^n} - \frac{1}{\rho_{i'}^n} \right) \tag{21}$$

$$b_n = \frac{1}{4\pi\epsilon_o} \sum_{i=1}^{N} \frac{2q_i \sin(n\phi_i)}{n} \left(\frac{1}{\rho_i^n} - \frac{1}{\rho_{i'}^n} \right) \tag{22}$$

when $n \geq 1$. The charges in the above equation are computed for unit applied potential difference between the pairs of electrodes of the trap. This is the convention followed in this work.[1]

Eqs. (21) and (22) have been used in conjunction with Eqs. (10) and (11) to calculate the multipole coefficients for our RITs. It should be noted that by the virtue of symmetry of the structure, the odd multipole coefficients, A_{2n+1} and all the B_n, are zero.

Verifications of the methods for calculating potential and multipole coefficients have been presented in the Appendices A.1 and A.2.

3.3. Trajectory calculation

The trajectories of ion motion were numerically obtained by using Runge Kutta fourth order integration. The force on the ion at point is obtained from the field computed using the BEM. The initial position and velocity of the ion are taken to be small and the integration is carried out for a prespecified (large) number of iterations. For plotting the ion trajectory, we use the position in x- and y-directions corresponding to each time step as the initial condition for the next step.

3.4. Stability region

For the 2D LIT, ion motion in the x- and y-directions can be described by the linear Mathieu equation and the stability plot can be generated by using the continued fraction expression which relates the parameters β_u, a_u and q_u [17]. For the RIT, this method of analytically calculating the stability region is not justified since the equations of motion in these traps are weakly nonlinear. Instead, we have adopted a numerical technique for doing this. In our method, for a given trap, for a chosen V_{rf}, a set of initial conditions corresponding to position and velocity of the ion in x- and y-directions and a U_{dc}, the trajectory of the ion is numerically generated for prespecified (large) number of iterations. If in these iterations the ion amplitude does not exceed the trap boundary in either x- or y-directions, ion motion is considered to be stable. To locate the instability at this chosen V_{rf}, U_{dc} is increased using a large step size and the ion motion is made unstable. After this initial crude identification of U_{dc} which results in ion destabilization (either the x- or y-directions), fine tuning of U_{dc} to identify its value at the stability boundary is carried out by a bisection method. This procedure is repeated for different values of V_{rf} till the entire stability region is covered. In our program a flag has been set to identify the direction in which ions are destabilized.

In order to convert the stability region obtained above on the U_{dc}– V_{rf} plane to one on the a_x– q_x plane, we use the Eq. (2) to obtain the a_x, q_x values for a pair of U_{dc}, V_{rf}.

In all numerically generated stability regions for the RITs on the U_{dc}– V_{rf} plane, we have superposed the Mathieu stability plot for an ideal LIT which has the same linear field (that is, the same a_2 as obtained from Eq. (21) with $n = 2$) as that of the RIT under study, for the purpose of comparison. In order to do this, we consider a symmetric LIT with hyperbolic electrodes, the distance from the centre to any electrode being $x_0 = y_0$. The potential in this LIT is given by $\Phi = a_0 + a_2(x^2 - y^2)$. The potential on the x-electrode is, therefore, $a_0 + a_2 x_0^2$, and on the y-electrode is $a_0 - a_2 x_0^2$. Since the potential difference between the electrodes is 1, $2a_2 x_0^2 = 1$. Consequently, for a given a_2 an LIT which generates the same a_2 can

[1] It should be noted, however, that some authors (for example, Collings [4], Douglas et al. [7]) report multipole coefficients obtained by applying a potential of +1 to one electrode pair and −1 to the other pair. This results in the numbers reported by them for the multipole coefficients being double those reported by us.

Table 2
Multipole coefficients obtained from BEM for RIT-S, RIT-X and RIT-Y

Multipole coefficients	RIT-S	RIT-X	RIT-Y
A_2	−0.5373	−0.6829	−0.6749

Normalizing length r_0 is 5 mm.

be found by choosing $x_0 = 1/\sqrt{2a_2}$. In the ideal LIT since the a_x–q_x stability plot is well known, U_{dc} and V_{rf} can be easily generated using Eqs. (2) and (21).

A verification of the method outlined above has been presented in the Appendix A.3.

3.5. Calculation of escape velocity

Escape velocity is the minimum velocity required for an ion, starting at the center of the trap, to escape from the trap [1].

To calculate the escape velocity of an ion of mass m at a chosen V_{rf}, we numerically integrate the ion motion using a set of initial conditions $(x, \dot{x})$, $(y, \dot{y})$. In our study the computations have been carried out for a single ion, for a range of rf voltage amplitudes with $U_{dc} = 0$. The rf phase angle was incremented in 16 steps of $\pi/8$, and angle of initial velocity in 6 steps of $\pi/3$ for each V_{rf}. From these 96 escape velocities values, the minimum was chosen for generating the escape velocity plots.

4. Results and discussion

4.1. Multipole coefficients

Multipole coefficients, A_2, which have been used in the present study are reported in Table 2 for the three RITs that have been investigated. These coefficients have been obtained using Eqs. (10) and (21).

4.2. Stability region

Figs. 5–7 show the stability regions for RIT-S, RIT-X and RIT-Y, respectively, on both the U_{dc}– V_{rf} as well as a_x– q_x planes. For generating these plots, the mass of the ion was taken to be 78 Th, r_0 as 5 mm, the rf drive frequency as 1 MHz ($\Omega = 2\pi \times 10^6$) and the initial conditions $(x, \dot{x})$, $(y, \dot{y})$ was taken as (0.001w m, 0.0 m/s), (0.001h m, 0.0 m/s), respectively, where w and h are the half-distance between the electrodes in the x- and y-direction, respectively. The values of A_2 for computing the corresponding a_x and q_x values in these plots were taken from Table 2 for the respective traps. The open circles represents ions which destabilize in the x-direction and the dots represents the ions that destabilize in the y-direction. Also superposed on these plots, with continuous lines, are the stability curves for the corresponding ideal LIT.

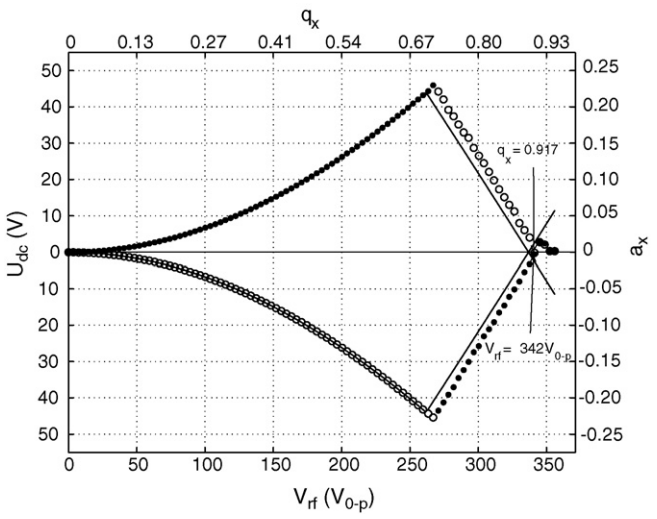

Fig. 5. Stability region for the RIT-S on the U_{dc}– V_{rf} and a_x– q_x planes.

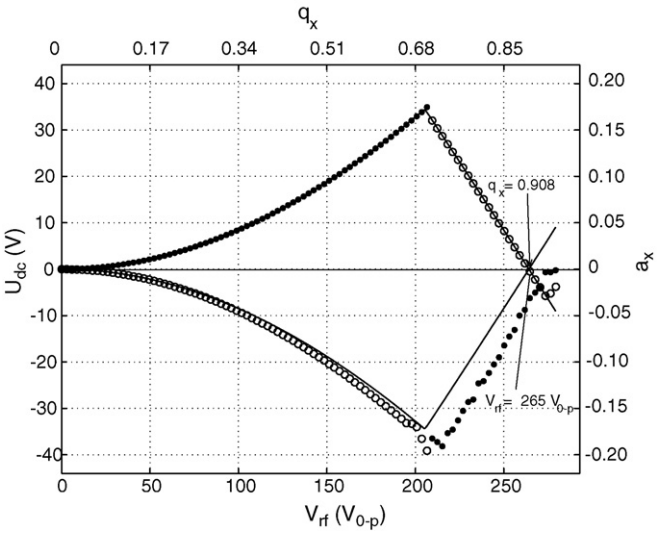

Fig. 6. Stability region for the RIT-X on the U_{dc}– V_{rf} and a_x– q_x planes.

4.2.1. Stability region for the RIT-S

Fig. 5 shows the stability boundaries for RIT-S as obtained by us numerically on the U_{dc}– V_{rf} and a_x– q_x planes. Indicated in the figure is the rf amplitude where the x- and y-stability curves intersect the $U_{dc} = 0$ line. It can be seen that both stability curves intersect the $U_{dc} = 0$ line at $V_{rf} \approx 342\,V_{0-p}$. Also superposed in the figure is the stability curve of the corresponding ideal LIT. For lower values of V_{rf}, the LIT curve and the numerically generated stability points for RIT-S are in close agreement and it is only at higher values of V_{rf}, beyond the apexes, that they deviate. In the ideal LIT, both the stability curves intersect $U_{dc} = 0$ line at $V_{rf} \approx 337\,V_{0-p}$, a value lower than $V_{rf} \approx 342\,V_{0-p}$ observed for the RIT-S. A delayed ejection is

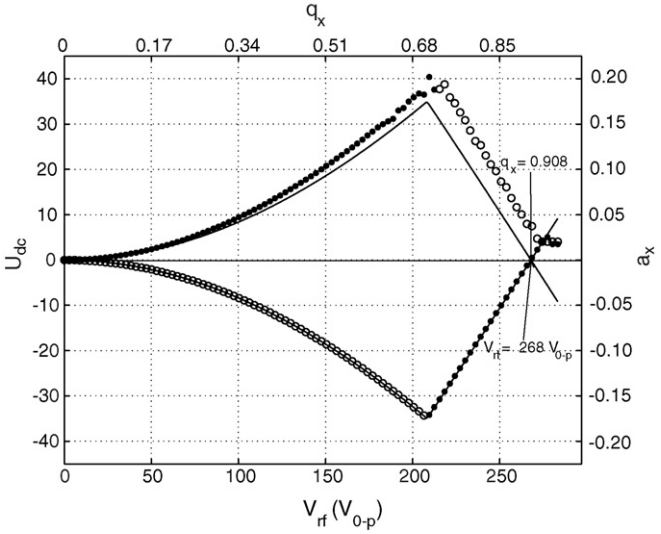

Fig. 7. Stability region for the RIT-Y on the U_{dc}– V_{rf} and a_x– q_x planes.

predicted for the RIT-S with $q_{cut-off} \approx 0.917$ and because both the x- and y-stability curves intersect the $U_{dc} = 0$ line simultaneously, ions will be equally predisposed to destabilize in the two directions.

We point out here an important difference between the results of our computations with the experimental results reported in Ouyang et al. [19] for a trap with somewhat similar parameters and operating conditions. While the V_{rf} at the stability boundary is close to $342\,V_{0-p}$ in our computations, they report an experimentally observed value close to $260\,V_{0-p}$. However, the results reported in our simulations compares favorably with the experimental results reported by Zhang et al. [32] for a slightly different geometry of the RIT which has $y_0 = 3.8$ mm.

4.2.2. Stability region for the RIT-X

Fig. 6 shows the stability region for the RIT-X (where the stretch is in the x-direction) on the U_{dc}– V_{rf} and a_x– q_x planes. This plot is in close agreement with the experimentally obtained stability boundary reported by Song et al. [27] for their 6-electrode RIT.

Two points need to be noted here. First is that the V_{rf} ($\approx 265\,V_{0-p}$) at which ions are destabilized, is considerably smaller than the corresponding value for the RIT-S (where V_{rf} was seen to be close to $\approx 342\,V_{0-p}$). The second point is that the x-stability curve crosses the $U_{dc} = 0$ line first, implying that the ion ejection will occur in x-direction preferentially in the mass selective boundary ejection experiment.

Comparison of this plot with the superposed plot of the corresponding ideal LIT makes for some interesting observations. It can be seen that three of the stability curves of the RIT-X closely match that the stability lines of the ideal LIT and it is the y-direction stability curve which shows considerable deviation. The deviation in the y-direction stability curve will not impact trap performance since it is the x-direction stability curve which will be encountered by the ions first in mass selective boundary ejection experiments. Consequently, not only will the ions preferentially destabilize in the x-direction but they will also destabilize at a V_{rf} close to the corresponding LIT. Our simulations show that the ion destabilization for the RIT-X occurs close to $q_x = 0.908$ unlike the delayed ejection suggested for the RIT-S.

4.2.3. Stability region for the RIT-Y

Fig. 7 shows the stability region for the RIT-Y on the U_{dc}– V_{rf} and a_x– q_x planes. The V_{rf} value at the stability boundary is close to $268\,V_{0-p}$ and in this case it is the y-stability curve which crosses the $U_{dc} = 0$ line first, implying that the ion ejection will occur in y-direction preferentially in mass selective boundary ejection experiments. As in the case of the RIT-X, the y-stability curve which crosses the $U_{dc} = 0$ line closely matches the corresponding curve of the ideal LIT. In this trap, two stability curves deviate from the corresponding LIT curves, but here too this should not impact trap performance in mass selective boundary ejection experiments since it is the y-direction stability curve which is first encountered by the ion. The ion destabilization for the RIT-Y occurs close to $q_x = 0.908$, a behavior similar to the RIT-X.

4.3. Escape velocity

The escape velocity simulations were carried out on a singly charged ion of mass 78 Th with initial conditions (x, $\dot{x}$) and (y, $\dot{y}$) being (0 m, 0.1 m/s) and (0 m, 0.1 m/s), respectively.

Figs. 8–10 are escape velocity plots for RIT-S, RIT-X and RIT-Y, respectively, along the V_{rf} axis. In these simulations U_{dc} was set to zero. Also indicated in the figure are the value of q_x.

The dips in the escape velocity plots are indications of nonlinear resonances within the trap and have the general form of the instability curves experimentally determined by Drakoudis et al. [8] for a

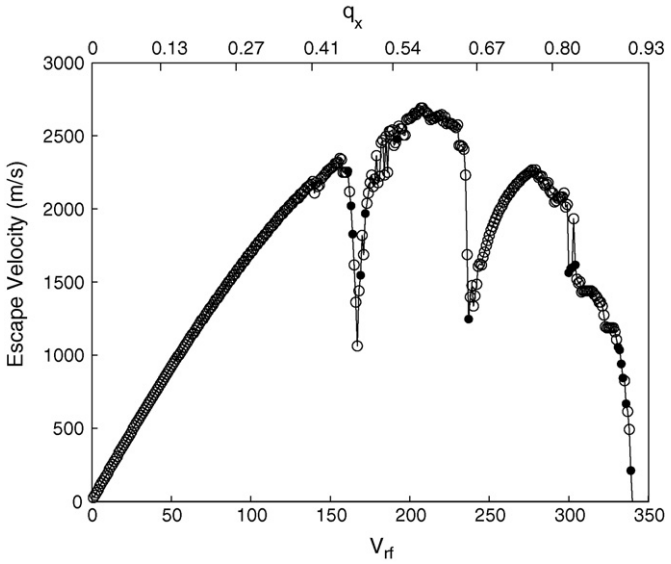

Fig. 8. Escape velocity plot for the RIT-S for different value of V_{rf}. q_x values are also indicated in the figure.

LIT with cylindrical electrodes. In the context of the RIT, one prominent resonance, which occurs close to $q_x = 0.64$ in all the plots, is due to octopole resonance and a detailed study of this resonance is presented in Abraham et al. [1]. The other prominent resonance close to 0.4 is the $\beta = 1/3$resonance, possibly due to dodecapole superposition. All others are combinational resonances involving sum and difference sideband frequencies of ion secular oscillations (as discussed in Franzen et al. [10]). Because of the top-bottom symmetry of the RITs assumed in our simulations, the experimentally observed resonance in the vicinity of $q_x = 0.8$ reported by Tabert et al. [30] will not appear in our simulations.

What is important to note in these figures is the direction of ejection of ions at different V_{rf} (or q_x) values. For the RIT-S, as seen in Fig. 8, escape predominantly occurs in the x-direction for most of the stable region of the trap operation. It is only close to the stability boundary, where the circles and dots are randomly distributed, our

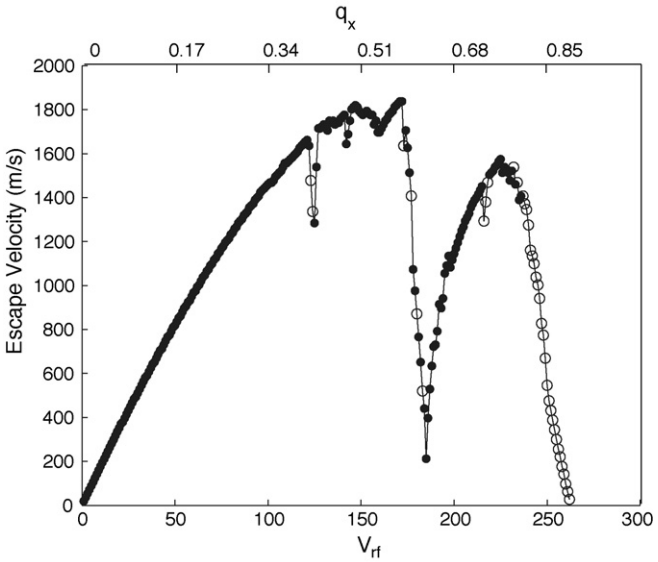

Fig. 9. Escape velocity plot for the RIT-X for different value of V_{rf}. q_x values are also indicated in the figure.

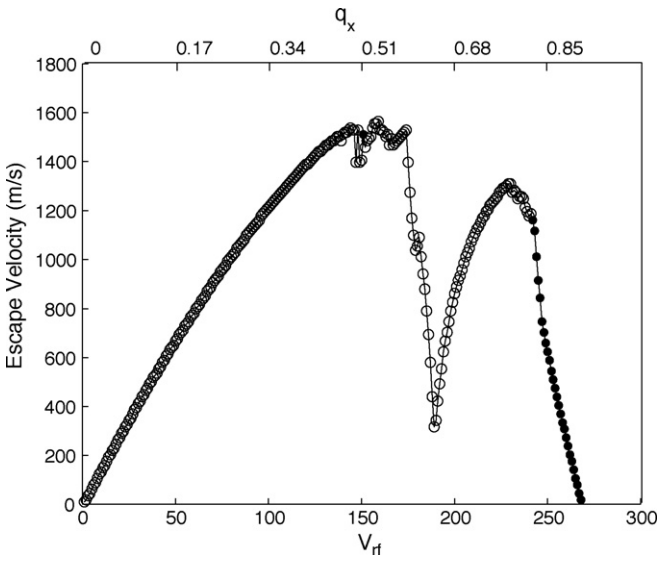

Fig. 10. Escape velocity plot for the RIT-Y for different value of V_{rf}. q_x values are also indicated in the figure.

simulations suggest that we see a mixed response and there is no definitive conclusion that can be drawn from this on directionality of ion ejection.

The picture is clearer for the escape velocity plots for the RIT-X (Fig. 9) which show very clearly that close to the stability boundary, escape takes place only in the *x*-direction, that is in the direction of the stretch of the trap. The picture is equally consistent for the RIT-Y, shown in Fig. 10, where at the stability boundary escape is seen to take place in the *y*-direction, the direction of the stretch.

4.4. The boundary ejection experiment

Our final simulation is the mass selective boundary ejection experiment to check for the direction in which the ion gets ejected from the trap. Unlike the resonance ejection experiment where the ion exit occurs in the direction of electrodes across which auxiliary ac excitation is applied, in the mass selective boundary ejection experiment carried out in our simulations, ions are free to destabilize in any direction they choose. Consequently, these experiments will enable us to get a further insight into the preferred directionality of ion ejection in these traps.

In the conventional experiment, a fragment ion is formed in the trap with a specific q_x value (which depends on the initial V_{rf} applied across the electrodes during ionization). Then, in order to mass selectively eject the ions from the trap, the V_{rf} is increased at a preset rate. When V_{rf} reaches a value corresponding to the stability boundary for the selected ion, ion ejection occurs.

In our simulations we have chosen an ion of mass 78 Th. The initial V_{rf} was fixed at 200 V_{0-p}. The V_{rf} was increased at a rate of 20V/200 μs (which is approximately 1 Th/200 μs). The initial conditions for the ion $(x, \dot{x})$ and $(y, \dot{y})$ was chosen to be (0 m, 0.1 m/s) and (0 m, 0.1 m/s), respectively. In order to cover all initial conditions under which the ion could be launched, its direction and rf phase were varied. In our simulations, both the velocity angle (which represents the direction) as well as the phase of the rf drive were varied in steps of 6 ° (60 steps in the velocity angle and 60 steps in the rf phase), giving a total of 3600 simulations. The direction (*x* or *y*) in which the ion amplitude reaches the trap dimension in the simulation is flagged in these simulations.

Table 3 presents the statistics we obtained for the RIT-S, RIT-X and RIT-Y on the 3600 simulations which were carried out on each of the RITs. Clearly, they follow the pattern and conclusions we reached in the earlier two simulations. The RIT-S shows that the ion is equally predisposed to go in either direction. The number 3 specified against the RIT-S, indicates the number of ions that got ejected through the gaps between the electrodes. In the case of the RIT-X and the RIT-Y, the clear preference of ion to go in the direction of stretch in evident.

Table 3
Table showing the statistics for the three configurations of the RIT

Configuration	*x* Electrode	*y* Electrode	Inter-electrode gap
RIT-S	1867	1730	3
RIT-Y	8	3592	0
RIT-X	3567	33	0

5. Concluding remarks

To investigate the directionality of ion motion in the RIT-S, RIT-X and RIT-Y, three numerical simulations were carried out for each of the RITs. In the first, we mapped the stability region of the trap on the U_{dc}– V_{rf} plane. This was done to check the direction of ion destabilization at the stability boundary along the $U_{dc} = 0$ line. In the second, we traced the escape velocity of the ions to verify the direction of ejection at the stability boundary. Finally, we simulated the mass selective boundary ejection experiment on the three RITs.

For the RIT-S, the three simulations indicated that ion destabilization occurs in both the *x*- and *y*-directions with roughly equal probability along the $U_{dc} = 0$ line. The picture was seen to be different for the stretched traps. For the RIT-X, all three simulations clearly indicated that ion destabilization occurred in the *x*-direction and for the RIT-Y, ion destabilization took place in the *y*-direction. These correspond to the direction of the stretch in these RITs.

A few interesting points emerge from the discussion presented above. First is in relation to the direction of ion ejection. It can be seen that for the RIT-S, the symmetric trap, the stability curves in the *x*- and *y*-directions simultaneously intersect the $U_{dc} = 0$ line. This implies that there is an equal probability for the ions being ejected in the two directions. For RIT-X and RIT-Y, on the other hand, the two stability curves intersect away from the $U_{dc} = 0$ line. In the case of RIT-X (Fig. 6), this intersection occurs below the $U_{dc} = 0$line, while for RIT-Y (Fig. 7), the intersection occurs above the $U_{dc} = 0$line. As a consequence, in mass selective boundary ejection experiments, for the RIT-X, it is the *x*-direction stability boundary that the ion encounters first, while for the RIT-Y, it is the *y*-direction stability boundary which is first encountered. This results in a preferential ejection of ions in the *x*-direction for RIT-X and in the *y*-direction for RIT-Y. In other words, the ions have a preferred direction for destabilization in stretched trap, the preferred direction being the direction of the stretch.

The second point that emerges from the simulations is in regard to the q_x value at the stability boundary. For the RIT-S, delayed ejection is predicted, with a $q_x \approx 0.917$. For the RIT-X and the RIT-Y, on the other hand, the observed situation is unexpected. For devices which are likely to have large nonlinear fields on account of the modified geometry, our simulations predict ion ejection at $q_x \approx 0.908$, which matches the nominal stability boundary of the linear LIT within the precision of our simulations. The respective stability boundaries for the RIT-X and RIT-Y also match closely with the corresponding curves for the ideal RIT.

Based on these numerical simulations we see that the detection sensitivity of the current instruments with one detector can be doubled by stretching the trap in the direction in which the detector is positioned. Here, because there is preferential ejection of ions in the direction of stretch, at least 50% of the destabilized ions will go

in the direction of the detector. The detection sensitivity can be further doubled if two detectors are used, with both being positioned on opposite electrodes in the direction of the stretch. However, four detectors are not expected, for stretched traps, to provide any significant advantage over two correctly positioned detectors.

Of course, in these instruments, there is no guarantee that all destabilized ions will exit through the slit (which is positioned at the centre of the electrode) to reach the detector, since several ions may hit the electrode wall. In order to maximize the number of ions getting through the slit, further work will be necessary to investigate modification of the shape of the electrodes to provide suitable ion optics which will guide ions through the slit.

Acknowledgement

We thank Anindya Chatterjee for discussions and suggestions on the manuscript.

Appendix A. Verification

To verify the accuracy of our numerical methods we have provided comparisons with a few results reported in literature.

A.1. Verification of potential calculation

In order to verify the correctness of the potential calculation, we compare our numerically obtained values with values obtained from an analytical expression. Fig. A.1 shows the arrangement of electrodes used for deriving the analytical expression for the potential within the structure. This set-up has plates arranged in form of a rectangle with potential applied as shown. The potentials applied provide the boundary values for a problem which is referred to as Dirichlet boundary value problem. This problem can be solved using the separation of variables method [14]. The geometry considered here is different to that of the RIT in that there is no spacing between the electrodes and there are no slits.

On solving Laplace equation for potential, $\Phi(x, y)$, using variable separable method, we get

$$\Phi(x,y) = \frac{1}{2} - \frac{4}{\pi}\sum_{k=0}^{\infty}(-1)^k \frac{\cosh((k+1/2)\pi x/h)\cos((k+1/2)\pi y/h)}{(2k+1)\cosh((k+1/2)\pi w/h)} \quad (23)$$

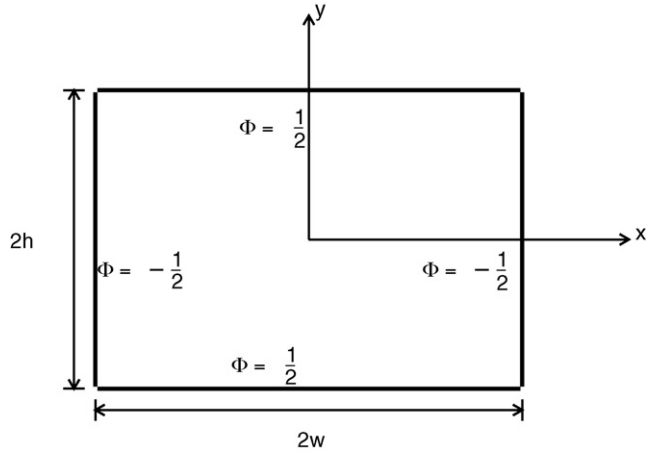

Fig. A.1. Diagram showing plates arranged as a rectangle with boundary conditions for comparing the approximate potential computed by the BEM with the separation of variables series solution.

Table A.1
Maximum difference in potential values calculated by the BEM and the analytical method

Number of divisions per electrode	Percentage difference
15	0.30
20	0.22
25	0.18
30	0.15

Table A.2
Comparison of coefficients obtained for the RITs reported by Ouyang et al. [19] with those obtained by us (BEM)

h	Ouyang et al. [19] A_2	BEM A_2
5.0	0.541	−0.5410
4.2	0.633	−0.6283
4.0	0.654	−0.6478

w is taken as 5.0 mm in all the three cases. Units of h are in mm.

In order to compare the potential obtained by BEM with those predicted by Eq. (23), we present in Table A.1 the maximum percentage difference in potential within an area of 80% of the central region of the structure. Column 1 of the table indicates the number of divisions per electrode in the BEM computations. It can be seen that although the accuracy increases with increasing number of divisions, the 20 divisions we have chosen in the present study is adequate.

A.2. Verification of multipole coefficients

Table A.2 presents a comparison of multipole coefficients obtained by BEM with the results reported by Ouyang et al. [19] for the three RITs they have investigated. The sign of the multipole coefficients obtained by BEM are opposite to that reported by Ouyang et al. [19] on account of the convention adopted by us being different from those adopted by Ouyang et al. [19]. The magnitudes of the multipole coefficients obtained by BEM match those obtained by Ouyang et al. [19].

Table A.3 presents a similar comparison with the multipole coefficients reported by Collings [4] for the trap in that study. Here the values computed match the values reported by Collings [4] with an accuracy of 10^{-3}. It should be noted that the convention used in Collings [4] with regard to the definition of multipole coefficients is to set the potential of +1 to one pair of electrodes and a potential of −1 to the other. It is for this reason that the A_2 values reported in Table A.3 are nearly double of the A_2 values reported in Table A.2.

In both cases the BEM provides a close match.

A.3. Verification of stability plot

To verify the numerical method developed by us for generating the stability plot, we compare the theoretical stability boundary of the ideal LIT with the numerically generated stability boundary using the method outlined in this paper.

Fig. A.2 presents the stability plot obtained by us numerically on the U_{dc}– V_{rf} plane (marking them with open circles and dots in the diagram) and by theoretical considerations (continuous line) discussed in Section 3.4.

Table A.3
Comparison of coefficients obtained from BEM with results reported by Collings [4]

	Collings [4]	BEM
A_2	1.001462	1.0029411

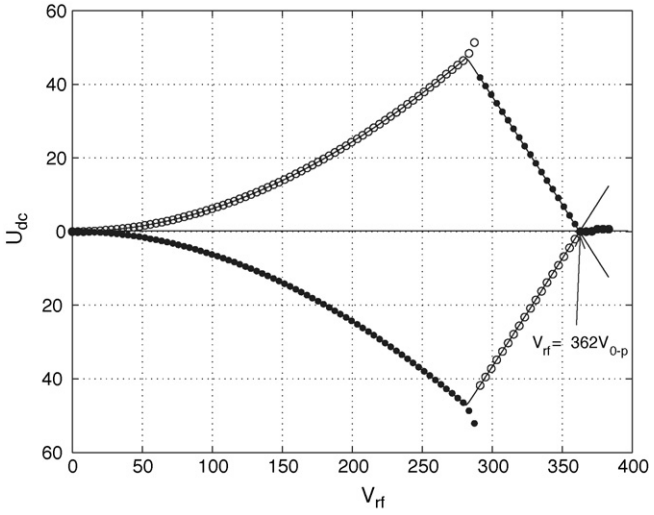

Fig. A.2. Numerically and analytically obtained stability plots for LIT-S.

As can be seen in the figure, the points obtained numerically are in close agreement with the line obtained by theoretical considerations, thus verifying numerical method adopted here.

References

[1] G.T. Abraham, A. Chatterjee, A.G. Menon, International Journal of Mass Spectrometry 231 (2004) 1.
[2] C.R. Arkin, B. Goolsby, D.A. Laude, International Journal of Mass Spectrometry 190-191 (1999) 47.
[3] M.E. Bier, J.E.P. Syka, U.S. Patent 5,420,425 (1995).
[4] B.A. Collings, Journal of American Society for Mass Spectrometry 16 (2005) 1342.
[5] P.H. Dawson, Quadrupole Mass Spectrometry and Its Applications, Elsevier, Amsterdam, 1976.
[6] G.G. Dolnikowski, M.J. Kristo, C.G. Enke, J.T. Watson, International Journal of Mass Spectrometry and Ion Processes 82 (1988) 1.
[7] D.J. Douglas, T.A. Glebova, N.V. Konenkov, M.Y. Sudakov, Technical Physics 44 (10) (1999) 1215.
[8] A. Drakoudis, M. Söllner, G. Werth, International Journal of Mass Spectrometry 252 (2006) 61.
[9] E. Fischer, Zeitschrift für Physik 156 (1959) 1.
[10] J. Franzen, R.H. Gabling, M. Shubet, Y. Wang, in: R.E. March, J.F.J. Todd (Eds.), Practical Aspects of Ion Trap Mass Spectrometry, vol. 1, CRC Press, New York, 1995, p. 69.
[11] J.E. Fulford, D.N. Hoa, R.J. Hughes, R.E. March, R.F. Bonner, G.J. Wong, Journal of Vacuum Science and Technology 17 (1980) 829.
[12] J.W. Hager, Rapid Communications in Mass Spectrometry 16 (2002) 512.
[13] J.V. Johnson, R.E. Pedder, R.A. Yost, Rapid Communications in Mass Spectrometry 6 (1992) 760.
[14] E. Kreyszig, Advanced Engineering Mathematics, John Wiley & Sons, New York, 2005.
[15] S.A. Lammert, W.R. Plass, C.V. Thompson, M.B. Wise, International Journal of Mass Spectroscopy 212 (2001) 25.
[16] F.A. Londry, J.W. Hager, Journal of The American Society for Mass Spectrometry 14 (2003) 1130.
[17] R.E. March, R.J. Hughes, Quadrupole Storage Mass Spectrometry, Wiley-Interscience, New York, 1989.
[18] A.C. Michaud, A.J. Frank, C. Ding, X.Z. Zhao, D.J. Douglas, Journal of the American Society for Mass Spectrometry 16 (2005) 835.
[19] Z. Ouyang, G. Wu, Y. Song, H. Li, W.R. Plass, R.G. Cooks, Analytical Chemistry 76 (2004) 4595.
[20] W. Paul, H. Steinwedel, U.S. Patent 2,939,952 (1960).
[21] N. Rajanbabu, A. Marathe, A. Chatterjee, A.G. Menon, International Journal of Mass Spectrometry 261 (2007) 170.
[22] J.C. Schwartz, 9th Sanibel Conference on Mass Spectrometry, Sanibel Island, FL (1997).
[23] J.C. Schwartz, M.W. Senko, J.E. Syka, Journal of the American Society for Mass Spectrometry 13 (2002) 659.
[24] M.W. Senko, J.C. Schwartz, A. Wieghaus, Operation of a linear quadrupole ion trap mass spectrometer under high space charge conditions, in: 51st ASMS Conference on Mass Spectrometry and Allied Topics, Montreal, CA, 2003, p. 8.
[25] S. Sevugarajan, A.G. Menon, International Journal of Mass Spectrometry 197 (2001) 263.
[26] Q. Song, S. Kothari, M.A. Senko, J.C. Schwartz, J.W. Amy, G.C. Stafford, R.G. Cooks, Z. Ouyang, Analytical Chemistry 78 (2006) 718.
[27] Y. Song, G. Wu, Q. Song, R.G. Cooks, Z. Ouyang, W.R. Plass, Journal of The American Society for Mass Spectrometry 17 (2006) 631.
[28] M. Sudakov, International Journal of Mass Spectrometry 206 (2001) 27.
[29] J.E.P. Syka, in: R.E. March, J.F.J. Todd (Eds.), Practical Aspects of Ion Trap Mass Spectrometry, vol. 1, CRC Press, New York, 1995, p. 169.
[30] M.A. Tabert, M.P. Goodwin, R.G. Cooks, Journal of The American Society for Mass Spectrometry 17 (2006) 56.
[31] E. Weber, Electromagnetic Fields: Theory and Applications. Vol 1 - Mapping of Fields, John Wiley & Sons, New York, 1950.
[32] C. Zhang, H. Chen, A.J. Guymon, G. Wu, G.R. Cooks, Z. Ouyang, 255–256 (2006) 1.
[33] G.C. Stafford, P.E. Kelley, J.E.P. Syka, W.E. Reynolds, J.F.J. Todd, Journal of Mass Spectrometry 60 (1984) 85–98.